Engineering Geology 197 (2015) 67–81

Contents lists available at ScienceDirect

Engineering Geology

journal homepage: www.elsevier.com/locate/enggeo

The influence of rock fabric in the durability of two sandstones used in the Andalusian Architectural Heritage (Montoro and Ronda, Spain)

E. Molina [a,*], D. Benavente [b], E. Sebastian [a], G. Cultrone [a]

[a] Department of Mineralogy and Petrology, University of Granada, Avda. Fuentenueva s/n, 18002 Granada, Spain
[b] Department of Earth and Environmental Sciences, University of Alicante, Carretera de San Vicente del Raspeig s/n, 03690 Alicante, Spain

ARTICLE INFO

Article history:
Received 3 October 2014
Received in revised form 6 April 2015
Accepted 8 August 2015
Available online 9 August 2015

Keywords:
Sandstones
Rock fabric
Petrophysical characterization
Porous system
Oriented textures
Durability

ABSTRACT

Natural stone has been a popular and reliable building material throughout history appearing in many historic monuments and in more recent buildings. Research into the intrinsic properties of specific stones is important because it gives us a greater understanding of the factors that limit and act on them. This can help prevent serious problems from occurring in our buildings bringing both esthetic benefits and financial savings. To this end, the main objective of this research has been to study the influence of the fabric and the mineral composition of two types of sandstone on their durability. The first is a red continental sandstone from the Buntsandstein Age called "Molinaza Roja", which is quarried in Montoro (Cordoba). The second is quarried in Ronda (Malaga) and is sold under the trade name of "Arenisca Ronda". It is a light pink-whitish calcarenite deposited during the Late Tortonian to Late Messinian. We characterized their petrological and petrophysical properties by studying their rock fabrics, porous systems and mechanical properties. In order to obtain a complete vision of the behavior of their rock fabrics, we also carried out two decay tests, the salt crystallization and the freeze–thaw tests. We then measured the effects on the textures of the altered samples during and after the decay tests and we evaluated the changes in the porous system. By comparing the results between intact and altered samples, we found that Arenisca Ronda is less durable because it has a high quantity of expandable clays (smectites) and a high percentage of pores in the 0.1–1 μm range, in which the pressure produced by salt crystallization is strongest. In Molinaza Roja the decay agents caused significant sanding due to loss of cohesion between the clasts, especially during the salt crystallization test. In both stones, the anisotropies (oriented textures) have an important role in their hydric and dynamic behavior and also affect their mechanical properties (especially in the compression resistance). No changes in color were detected.

1. Introduction

Extensive research has been done on the characterization and behavior of building materials, something that has direct benefits in terms of the better use of available resources, and of improved behavior of the stone once it forms part of the building (Cultrone et al., 2007; Dunford et al., 2012; Gutiérrez et al., 2012; Lombillo et al., 2013; Miranda et al., 2012; Moropoulou et al., 2000; Vereecken and Roels, 2013; Xiao et al., 2014). Of the various building materials that have been used since ancient times, stone is undoubtedly the most widely used (Fort, 2008), if we bear in mind that it is normally more durable than the other materials. In other words it has a greater capacity to resist possible alterations caused by different environmental agents without its quality being impaired or changes in its shape or size over a long period of time (Bell, 1993).

The "imperishable" (at least in principle) nature of natural stone has made it a material of choice in the construction of historic monuments in certain cities to the extent that it has often become an essential feature of a particular architectural style. Indeed mankind has used stone throughout his evolution from the earliest most primitive stone tools or as a surface on which to paint and for erecting magnificent civil and above all political and religious buildings. However due to the lack of scientific research into the materials, our knowledge of the durability of different stones has until recently been largely based on the empirical evidence acquired by craftsmen and their observations over successive generations. Durability has often been affected by the action and concentration of external atmospheric agents, which have damaged or deteriorated its original properties (Cámara et al., 2008; Langella, 2000; Massey, 1999; McCabe et al., 2009; Mulvin and Lewis, 1994; Prieto and Silva, 2005). Since the Industrial Revolution and especially from the 20th Century onwards, these decay processes have in many cases been exacerbated and accelerated (Fort, 2009), including those caused by atmospheric pollution (Massey, 1999; McAlister et al., 2006, 2008).

A wide range of stones are used as building materials in the Iberian Peninsula (Fort, 2008; Roc Máquina, 2013) most of which are relatively easily accessible. It is therefore hardly surprising that in many towns and villages almost all the architectural heritage is made of stone. In

* Corresponding author.
E-mail address: molinap@ugr.es (E. Molina).

http://dx.doi.org/10.1016/j.enggeo.2015.08.009
0013-7952/

addition certain types of stone have been used for one specific purpose for which they have certain properties that make them ideal. These include for example the use of phyllites and schists in roofs (Cárdenes et al., 2012, 2014; Fasana and Nelva, 2013) or the use of marble as a material as a means of showing high social and economic status (Luque Aranda, 2010).

In many cases because marble has been considered a more "high-class" material or because it has been more widely used, it has also been a more popular subject for research, such that it is relatively easy to find information about the composition and properties of different kinds of marble with the resulting benefits in terms of better conservation and use (Luque Aranda, 2010; Rodríguez-Gordillo and Sáez-Pérez, 2006; Siegesmund et al., 2000; Steiger, 2005). Other materials, by contrast, have received much less attention, to the extent that no scientific research has been conducted on them despite their use in building. This explains at least in part why in buildings and monuments that are suffering serious decay processes, the causes are unknown and restorers do not know what best to do to counteract the damage or prevent future damage from occurring.

With this in mind, in our research we have selected two lithotypes known as "Molinaza Roja" and "Arenisca Ronda", which are relatively unknown from a scientific point of view despite being extensively used in the towns of Montoro and Ronda (southern Spain), respectively. Almost no scientific research has been done on Arenisca Ronda, while Molinaza Roja has only been analyzed on a few occasions (Clementson Lope, 2012; Clementson Lope et al., 2007, 2009; Molina et al., 2011a). Both cities have many stone-built heritage buildings of great historic and artistic interest. In fact in these cities these stones are not only used in political and religious buildings, and can also be seen in many houses and urban decoration (cobbles, façades, benches, fountains, etc.), giving the town as a whole an unarguable visual impact due also to the fact that each variety has a very characteristic color tone. In Montoro, there are valuable examples of the use of Molinaza Roja such as the Bridge of the Donadas, the churches of San Bartolomé, Santiago and San Juan de Letrán, the Hospital of Jesús Nazareno, the city council, the bullring and in the paving of some of the town's squares. In Ronda, interesting examples of the use of Arenisca Ronda include the New Bridge, the Islamic walls, the churches of Padre Jesús, Santa Catalina and Espíritu Santo, the Town Hall, the bullring and in various palaces, such as in the Palace of the Marqueses de Moctezuma or that of the Marqués de Salvatierra.

A wide range of analytical techniques can be applied in the characterization of a stone material (Esbert et al., 1997), with scientists' deciding which ones they want to use on the basis of their particular objectives. In order to make a complete study of the influence of the fabric of a rock on its durability, it is necessary to combine the results of various techniques, so as to obtain a clearer vision of the factors and characteristics that can influence or limit the durability of the stone used in construction (Molina et al., 2013). In this sense, a mineralogical study using X-ray diffraction can provide information about the minerals that make up the rocks and the possible presence of potentially damaging phases such as salts or swellable clays even when present in low concentrations. The identification of mineral phases can be completed by other analytical techniques such as optical and electronic microscopy, techniques which can also be used to characterize the texture and microtexture. This will give us some idea of the degree of union between the crystals, the empty spaces (pores, fissures, fractures) and the anisotropies in the stone (sedimentary structures, preferential orientations, stylolites, etc.). We can take the porosity observed under the microscope a stage further by using mercury injection porosimetry to find out the size and distribution of the pores, important information in that these are the main paths through which the pollutants enter and circulate around the stone (Dunning and Huf, 1983; Franzen, 2004; Molina et al., 2011b). In order to extend this information it is also advisable to perform hydric tests and establish a series of coefficients that indicate the relative ease or difficulty with which fluids circulate inside the rock (Alonso, 1986; Esbert et al., 2008). Given that the pores and fissures are also the preferred paths for the circulation of chemical and physical decay agents, the standardized salt-crystallization and freeze–thaw aging tests allow us to assess in a short space of time the damage that these materials would suffer as a result of aging (Bayram, 2012; Espinosa et al., 2008) and compare them with the damage observed in the buildings (Grossi et al., 2007; Laycock, 2002). Finally, the measurement of the velocity of propagation of ultrasonic waves allows us to assess the degree of compactness of a rock, as the speed of propagation depends directly on the percentage of the pores, the type and volume of the fissures, the density and composition of the minerals, the textural anisotropy and the humidity present (Barbera et al., 2012; Fort et al., 2011; Simmons, 1965). The results obtained can then be compared and completed with mechanical studies.

The main objective of our research is therefore to compare the petrographic and physical properties of two rocks used in the construction of historic buildings in Andalusia (Spain), Molinaza Roja and Arenisca Ronda, in order to determine how their fabric influences their durability and in this way predict or prevent their decay once in place in the building. For this purpose, using samples from the quarry we will be characterizing the fabric of each variety, by studying their mineralogy, texture, porous system, hydric parameters, mechanical resistance, dynamic properties and color. We will then subject the samples to accelerated aging tests, after which we will measure some of the above parameters again. We will then compare the results with those for the original intact samples and so discover the strengths and weaknesses of each stone. Although these rocks are not used together because of their different mineralogical and textural characteristics, the results of our comparative study could prove useful for architects and builders in Andalusia when choosing which type of rock to use in stone constructions. The methodology we follow could also serve as a model for research into other building stones with similar features.

2. Materials selected and geological settings

The sandstones from Montoro (Cordoba) and Ronda (Malaga) selected for this study are widely used in old and new buildings in the two cities and both are currently quarried.

2.1. The "Molinaza Roja" (MR)

The "Molinaza Roja" (MR) is a sandstone quarried near to the town of Montoro (Cordoba). The quarry (Fig. 1) is located 2–3 km northwest of the city. The color of the stone varies from red to purple (Fig. 1–a), due to the alternating lamination rich in iron oxides and hydroxides (Clementson Lope et al., 2009). The clasts are less than 1 mm in size. The pores are difficult to distinguish to the naked eye.

This material is a red continental sandstone deposited in fluvial and alluvial environments during Buntsandstein and corresponding with Red Bed facies (Gibbon and Moreno, 2002). These Triassic materials are discordant with respect to the Paleozoic materials (Fernández and Gil, 1989). They are laid out in alternating strata between clays and sandstones. The arkose layers are of higher quality (Clementson Lope et al., 2007) for the use in construction than the greywackes layers. We therefore decided to focus exclusively on the arkose layers.

2.2. The "Arenisca Ronda" (AR)

The "Arenisca Ronda" (AR) is a sandstone quarried (Fig. 1) 4–5 km to the northeast of the city of Ronda (Malaga). It is a carbonate sandstone and the mean size of the clast is usually around 1–2 mm (Fig. 1–b). AR is a light pink-whitish stone, the rock fabric is massive and only in some cases can clast orientation be detected.

The Ronda Basin is one of the largest piggyback basins in the Western Betics. It is located over the north-western Subbetic Units with a continuous structure, the Subbetic Chaotic Complexes and the Flysch

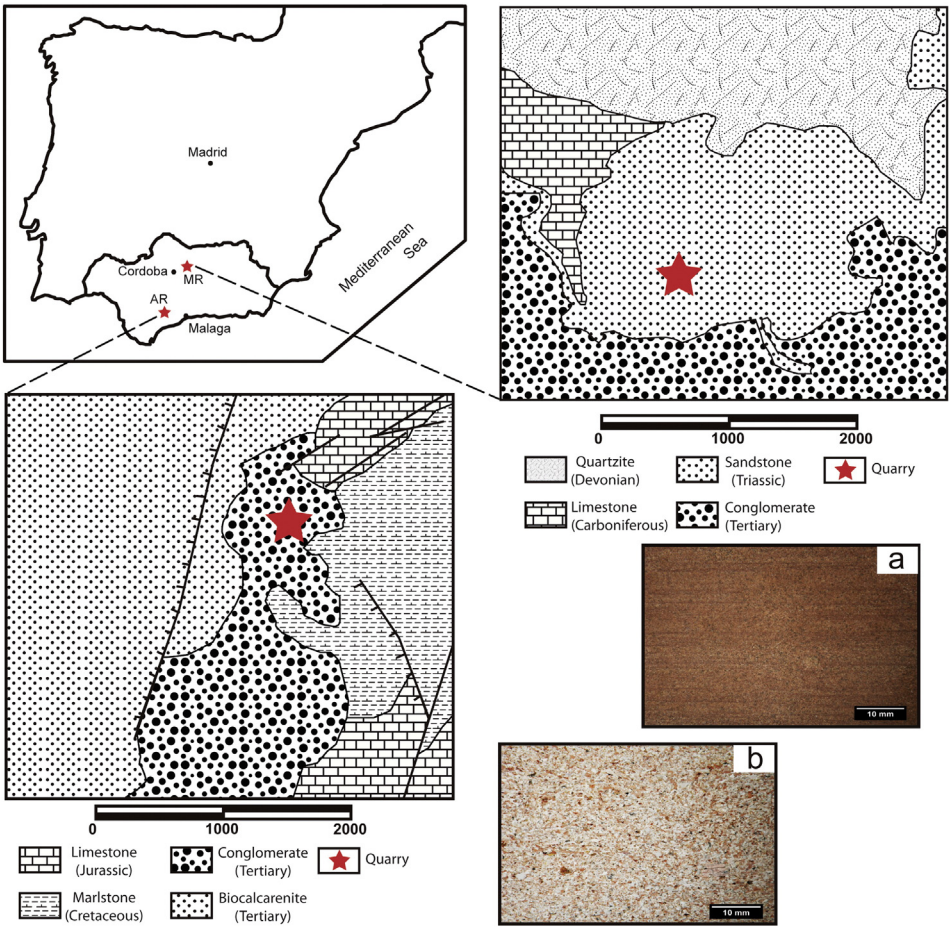

Fig. 1. Location of the towns and the present-day quarries in Montoro (MR) and Ronda (AR) and the geological maps for Molinaza Roja (modified from Armengot de Pedro et al. (1972)) and Arenisca Ronda (modified from del Olmo Sanz et al. (1981)). A detailed image of the oriented textures of Molinaza Roja (a) and Arenisca Ronda (b) is also shown. (For interpretation of the references to color in this figure, the reader is referred to the web version of this article.)

Units (Ruíz-Constán et al., 2008; Viseras et al., 2004). The sedimentary infill is Late Miocene in age and was divided into four different formations by Serrano (1979) and Rodríguez-Fernández (1982). The Setenil Formation on the top is Late Tortonian to Late Messinian in age and crops out in most of the depression. Rodríguez-Fernández (1982) divided this formation into two members, the limestone member and the calcarenite member, in which AR is quarried.

3. Experimental procedure

The following sections have been divided into the characterization of unaltered stones (referred to as intact stones) and then after aging tests referred to as altered stones.

3.1. Properties of intact stones

3.1.1. Mineralogical and petrographic study

The mineralogical composition of the two sandstones was determined by the X-ray diffraction technique (XRD), with which we analyzed the entire samples and the clay (below 2 μm) fraction. To identify the mineralogy of the samples, we milled them in an agate mortar and analyzed the powder with a Philips X'Pert PRO diffractometer. The following working conditions were applied: radiation CuKα ($\lambda = 1.5405$ Å), voltage 45 kV, current 40 mA, scanning angle 3–60° 2θ and goniometer speed 0.1 2θ s^{-1}. To determine the clay fraction, we ground 100 g of sample of each stone and placed it in a beaker with deionized water. The samples were then treated during several cycles with acetic acid (CH_3COOH) with a concentration of 1 N to eliminate the carbonates until no reaction process was observed. The samples were then washed several times to eliminate the acid in the water and hydrogen peroxide (H_2O_2) at 20% volume was added to eliminate any possible organic matter. After that we added sodium hexametaphosphate to separate the aggregates that may have formed. Samples were concentrated by removing excess water and we separated the fraction below 2 μm using a Kubota KS-8000 centrifuge. Once we had obtained the clay fraction, we deposited it on glass sample-holders using the oriented aggregate method (OA). We also prepared oriented aggregates in order to solvate them for 48 h at 60 °C with ethylene-glycol (AO-EG) (Bruton, 1955), so as to determine the presence of swellable clays; with dimethyl-sulfoxide for 72 h at 80 °C (AO-DMSO) (González García and Sánchez Camazano, 1968) to identify the kaolinite phase; and to heat them at 550 °C for 90 min (AO-550) (Moore and Reynolds, 1989) to check whether they contain chlorite. Each OA was analyzed using the same conditions as for raw material, except for the scanning angle that ranged between 3 and 30° 2θ. We interpreted X-ray diffraction patterns using the XPowder© software v.12 (Martín Ramos, 2004).

We completed the mineralogical analysis of the samples by observing their texture. When observing textural differences between rocks, it is important to take into account the orientation of the lamination (Choquette and Pray, 1970) and the morphology, abundance, size and distribution of the pores and fissures must also be assessed. To this end we prepared six thin sections (two for each orthogonal direction, according to their sedimentation planes) per stone to be observed under a CarlZeiss Jenapol-U polarized optical microscope (POM) equipped with a digital microphotography unit (Nikon D7000). The thin sections were stained with alizarin to identify the calcite more

clearly from the other carbonated minerals. We then examined the thin sections under a Leo Gemini 1530a field emission scanning electron microscope (FESEM) in BSE mode to observe the microtexture of Molinaza Roja and Arenisca Ronda. In this way, the resolution quality of the POM technique was completed with that of FESEM, and the relationship between clasts and pores was studied at different ranges, using POM to study the range from 1 mm to 1 μm and FESEM for detailed observation down to 0.1 μm.

3.1.2. Chemical composition

The chemical composition of each stone was analyzed by means of X-ray fluorescence (XRF) and the content was expressed as the oxide weight (wt.%) normalized to 100% of the major and minor elements, LOI-free (corrected for "Loss On Ignition"). Samples weighing 5 g were finely ground and well mixed in an agate mortar before being pressed into an Al holder for disc preparation. ZAF correction (a generalized algebraic procedure that takes into account the atomic number-Z-, the absorption-A- and the fluorescence-F- of the elements) was performed systematically (Scott and Love, 1983), and the NCS DC 74301 (GSMS-1) standard was applied and ten major and minor elements were measured (Chen and Wang, 1998). The estimated accuracy for major elements is below 6%, except for K (8%). The precision was lower than 1%, except for Mn, which shows values ranging from 1.35 to 1.62% (Niembro Bueno, 2009).

3.1.3. Characterization of porous system and hydric behavior

The open porosity (P_{MIP}) and the pore size distribution of the stones were evaluated by mercury intrusion porosimetry (MIP) using a Micromeritics Autopore III porosimeter, model 9410, which can generate a pressure of 414 MPa, covering the pore diameter range from approximately 0.003 to 360 μm. Freshly cut sample chips of about 1 cm^3 were oven-dried for 24 h at 100 °C and then analyzed. Three MIP measurements were made per lithotype. We also obtained the bulk (ρ_b) and skeletal density (ρ_{sk}). To obtain the total porosity (P_T), three measurements of their true density (ρ_t) were made per lithotype on samples of 20 × 20 × 30 mm which were oven-dried for 24 h at 100 °C before the measurement. We used a Micromeritics AccuPyc 1330 helium pycnometer and the P_T was calculated as follows:

$$P_T = \left(1 - \frac{\rho_{bT}}{\rho_T}\right) \times 100,$$

where ρ_{bT} is the dry bulk density of the stone, defined as the ratio of its mass to its volume, including the volume of voids and grains. The true density, ρ_T, is defined as the ratio of its mass to solid volume.

The nitrogen adsorption technique was used to complete the porometric analysis in the nano-micropore range using a Micromeritics Tristar 3000 apparatus which approximately covers the 0.002–0.05 μm pore range. N_2 isotherms were obtained at 77 K. BET analysis (The Brunauer–Emmett–Teller theory explains the physical adsorption of gas molecules on a solid surface) was used to calculate the specific surface area of the samples, while pore size distribution curves were obtained using the Barrett–Joyner–Halenda (BJH) method (a procedure for calculating pore size distributions from experimental isotherms using the Kelvin model of pore filling) (Gregg and Sing, 1982).

To obtain a complete vision of the porous system of the stones, we carried out hydric tests (HT) using four samples per lithotype with a cubic shape and 5 cm-edge. We used the UNE-EN 1936 (2007) standard to determine the open porosity (P_{HT}) and the bulk (ρ_{Hb}) and skeletal (ρ_{Hsk}) densities as follow:

$$P_{HT} = \frac{M_S - M_0}{M_S - M_H} \times 100;$$

$$\rho_{Hb} = \frac{M_0}{M_S - M_H};$$

$$\rho_{Hsk} = \frac{M_0}{M_0 - M_H},$$

where M_0 is the mass of the dried sample, M_S is the mass of the sample saturated with water under vacuum and M_H is the mass of the sample saturated with water under vacuum and weighted in water.

Hydric tests were useful to determine the free (A_b, at atmospheric pressure) and forced (A_f, under vacuum) water absorption values following the UNE-EN 13755 (2008) standard and the drying index (D_i) (NORMAL 29/88, 1988). We also determined the degree of interconnection between the pores (A_x) (Cultrone et al., 2003) and the saturation coefficient (S) (RILEM, 1980). These parameters were calculated as follows:

$$A_b = \frac{M_L - M_0}{M_0} \times 100;$$

$$A_f = \frac{M_S - M_0}{M_0} \times 100;$$

$$Di = \frac{\int_{t_0}^{t_f} f(M_t)dt}{M_S \times t_f};$$

$$A_x = \frac{A_f - A_b}{A_f} \times 100;$$

$$S = \frac{M_{48h} - M_0}{M_S - M_0} \times 100,$$

where M_L is the mass of the sample saturated with water at atmospheric pressure (until constant mass is reached), M_{48h} is the mass of the sample after 48 h immersion in water at atmospheric pressure, M_t represents a decreasing water weight content as a function of time and t_0 and t_f are respectively the start and end times for the test.

To determine the capillarity coefficient (C_c) and the capillarity height (H_c) of samples the capillary test was carried out on three cube samples per stone type (5 cm edge) following the UNE-EN 1925 (2000) standard. The capillarity coefficient was obtained by measuring the slope of the initial straight line of the water absorption curves by capillarity:

$$C_C = \frac{M_t - M_0}{A\sqrt{t}},$$

where M_t is the amount of water absorbed at time t and A is the surface of the sample in contact with water. We also calculated the height of water rise by capillarity *h* at time *t* as follows:

$$H_C = \frac{h}{\sqrt{t}}.$$

In view of the fact that the bedding planes of MR appear well defined to the naked eye and a preferred orientation of the grains can be detected in AR in some cases, we decided to perform the capillarity tests on samples with both perpendicular (C_{C1} and H_{C1}) and parallel (C_{C2} and H_{C2}) orientations to these planes.

Finally, we studied the movement of water vapor inside the pore system measuring the vapor permeability coefficient (K_v) according to the NORMAL 21/85 (1985) standard. Three samples measuring 4 × 4 × 2 cm were used per stone. This coefficient was obtained by the slope of the straight line of water vapor transfer:

$$K_v = \frac{\Delta M/A}{t},$$

where ΔM is the amount of water vapor transfer at time t, and A is the surface of prismatic samples 1 cm thick. We used three samples per

stone and temperature was maintained constant during the test at 20 °C.

3.1.4. Dynamic properties

The compactness of the stone was evaluated by ultrasounds using a Panametrics HV Pulser/Receiver 5058PR coupled with a Tektronix TDS 3012B oscilloscope under controlled thermo-hygrometric conditions (~20 °C and relative humidity of ~35%). The measurements were performed on 15 cube samples per stone (5 cm edge) and in three orthogonal directions: direction 1 perpendicular to the sedimentation planes and directions 2 and 3 parallel to them. In accordance with the ASTM D 2845-05 (2005) standard, the propagation velocity of compressional (V_p, in m/s) and shear (V_s, in m/s) pulses was measured for dry test samples using polarized Panametrics transducers of 1 MHz with a contact surface of 3 cm in diameter. We used a viscoelastic couplant (an ultrasound eco-gel) to obtain a good coupling between the transducers and the stone surfaces. The transmission method was used and three measurements were taken for each orthogonal direction of the samples. We calculated the Poisson coefficient (ν) and the Young (E, in GPa), shear (G, in GPa) and bulk (K, in GPa) modules, which are useful to predict the deformation behavior of building materials (González de Vallejo et al., 2002) with the following equations:

$$\nu = \frac{(V_P/V_S)^2 - 2}{2\left[(V_P/V_S)^2 - 1\right]};$$

$$E = 2\rho_b V_S^2(1+\nu);$$

$$G = \frac{E}{2(1+\nu)};$$

$$K = \frac{E}{3(1-2\nu)},$$

where ρ_b is the apparent density previously determined by MIP. V_p values were also useful for defining the total (ΔM) and relative (Δm) anisotropies (Guydader and Denis, 1986) as follows:

$$\Delta M = \left(1 - \frac{2V_{pmin}}{V_{pmax} + V_{pmean}}\right) \times 100;$$

$$\Delta m = \frac{2(V_{pmax} - V_{pmean})}{V_{pmax} + V_{pmean}} \times 100,$$

where V_{pmax} is the mean maximum velocity, V_{pmin} is the mean minimum velocity, and V_{pmean} is the mean intermediate velocity in any one of the three orthogonal directions.

3.1.5. Mechanical properties

We performed the uniaxial compression test following the UNE-EN 1926 (2007) standard using six cube-shaped samples with 5 cm-edge for each stone. The samples were positioned with their stratification planes or bands, perpendicular and also parallel to the direction of the load. The compressive strength (R_c, in MPa) was calculated according to the following formula:

$$R_c = \frac{F}{A},$$

where F is the break load (in N) and A is the area of the transversal section of the sample before testing (in mm^2).

The information about the mechanical properties was completed carrying out the flexural test (UNE-EN 12372, 2007). The samples measured 20 × 5 × 3.2 cm and six were used for each stone. The flexural strength (R_{tf}, in MPa) was calculated as follows:

$$R_{tf} = \frac{3Fl}{2bh^2},$$

where F is the load (force) at the fracture point (in N), l is the distance between the support span (in mm), b is the width (in mm), and h is the thickness of the sample (in mm).

3.1.6. Spectrophotometry

We characterized the color of the samples by spectrophotometry. The UNE-EN 15886 (2011) standard was followed and a Konica-Minolta CM-700d spectrophotometer was used. The CIELab system was chosen and L* (lightness) varying from black with a value of 0 to white with a value of 100 and chromatism parameters (from −60 to +60) where a* varies between +a* (red) and −a* (green) and b* varies between +b* (yellow) and −b* (blue) were calculated using reflectance values. The measurement conditions were: a measurement area of 8 mm, D65 standard illuminant and observer 10° with modes SCI/SCE and a wavelength range from 400 to 700 nm with a wavelength interval of 10 nm. Fifteen measurements per stone were performed. Color difference ($\Delta E_{94}{}^*$) was calculated with the following equation (UNE-EN 15886, 2011):

$$\Delta E_{94*} = \left(\left(\frac{\Delta L*}{k_L \cdot S_L}\right)^2 + \left(\frac{\Delta C*}{k_C \cdot S_C}\right)^2 + \left(\frac{\Delta H*}{k_H \cdot S_H{}^H}\right)^2\right)^{1/2}.$$

The factors (S_L, S_C y S_H) and the variables (k_L, k_C y k_H) in this equation weigh and correct the amplitude of the difference of color perceived by modifying the lightness (L*), the chromatism (C*) and the tone (H*) of the chromatic space L*a*b*.

3.2. Evaluating the durability of the stones

3.2.1. Decay tests

Freeze–thaw and salt crystallization tests were carried out to evaluate the decay suffered by MR and AR stones. These tests were selected because they are the most frequently used and the most aggressive tests for assessing stone decay in the laboratory. The degree of deterioration was controlled by measuring the weight changes (wt.%) every cycle and the loss of fragments along the edges which had been painted prior to the experiment to facilitate the observation of damage. The

Table 1
Mineralogical composition of raw (in %) and clay fraction (%) of Molinaza Roja (MR) and Arenisca Ronda (AR). Legend: Qz, quartz; Cal, calcite; Dol, dolomite; Ms, muscovite; Fsp, feldspar *s.l.*; Chl, chlorite; Gth, goethite; Ilt, illite; Sme, smectites; Kln, kaolinite (mineral symbols after Whitney and Evans (2010)). The values indicated in "%fraction" are the percentage of each compound, where CF is the percentage of the clay fraction (<2 μm), IR is the insoluble residual (>2 μm) and CB is the carbonates content. The amount was expressed as follows: tr, traces; –, absent.

	Raw fraction							Clay fraction (CF < 2 μm)				% Fraction		
	Qz	Cal	Dol	Ms	Fsp	Chl	Gth	Ilt	Sme	Chl	Kln	CF	IR	CB
MR	>80	3	tr	3	14	tr	tr	>80	tr	5	10	0.8	≈98	<1
AR	tr	>95	tr	–	–	–	–	7	72	–	20	2	≈6	≈92

Table 2
Chemical composition of Molinaza Roja (MR) and Arenisca Ronda (AR). Major and minor elements are expressed in wt.%.

	Major and minor elements										
	SiO_2	Al_2O_3	Fe_2O_3	MnO	MgO	CaO	Na_2O	K_2O	TiO_2	P_2O_5	LOI (%)
MR	67.13	13.07	2.04	0.14	1.93	5.08	0.18	6.14	1.04	0.262	2.45
AR	3.89	1.59	0.59	0.07	0.35	59.36	0.02	0.19	0.06	0.079	33.3

UNE-EN 12371 (2011) standard was followed for the freeze–thaw testfor which 25 cycles (of 24 h each cycle) were carried out. We used four samples per stone with a cube shape and a 5 cm-edge. The damage caused by salts was analyzed according to the UNE-EN 12370 (2002) standard. For this test, four cube-shaped 5 cm-edge samples were used per lithotype and 15 cycles (of 24 h each cycle) were carried out using a solution of 14% $Na_2SO_4 \times 10H_2O$. The environmental conditions in the laboratory were 20 °C and 30% ±5 of relative humidity in both tests. Samples were placed with the lamination parallel to the base.

To complete the information about the durability of the stones and the degree of alteration, we repeated some of the tests during or after the deterioration of the samples. For this purpose, MIP analyses were carried out after freeze–thaw and salt crystallization tests to determine the changes in the porous system during decay of the stones. In the case of samples altered by salt, we measured the porosity after removing the salt from the samples. The changes in the texture were evaluated by means of ultrasound measurements after every five cycles in both decay tests. In the samples subjected to the freeze–thaw test, ultrasound measurements were conducted on water saturated samples before they were put in the freezer. Water-saturated samples were used so as not to interrupt the test and to avoid prolonging it excessively. In the samples subjected to the salt-crystallization test, the ultrasound measurements were conducted on dry samples before they were put in the saline solution. We evaluated the color differences ($\Delta E_{94}{}^*$, UNE-EN 15886 (2011)) between intact and altered stones by spectrophotometry. Finally, small fragments (of approximately 1 cm^3) from altered samples were analyzed using environmental scanning electron microscopy (ESEM). The aim of this analysis was to evaluate whether the texture had been affected by salt or ice crystallization. For this we used a Quanta 400 microscope coupled with energy dispersive x-ray microanalysis (EDX) in BSE mode.

4. Results and discussion

4.1. Rock fabric and mineralogical characterization in intact stones

4.1.1. Mineralogical, chemical and petrographic description

Table 1 shows the mineralogical composition as determined by XRD for each rock expressed in percentages. In the Molinaza Roja (MR) sample, quartz is the main mineral phase (>80%), while feldspar, above all potassium feldspar, has been discovered in smaller quantities. Other phases identified with concentrations from low to traces were in descending order, calcite, dolomite, muscovite, chlorite and goethite. In the case of Arenisca Ronda (AR), calcite is the foremost mineral phase (>95%) and quartz was observed in very low quantities or in traces.

As regards the clay fraction (Table 1),we found that the most abundant mineral phases in MR are illite (>80%) and in smaller proportions of chlorite, while in AR the percentage of illite is much smaller than that of smectite and kaolinite. The possible presence of swellable clays such as smectites has important implications for the durability of the rock due to their adverse effects on the swelling-drying processes, causing additional strain in the rocks and damaging their original physical and mechanical properties. In our case study AR has a high concentration of smectites (about 70%) compared to MR where it appears only in traces. This must be borne in mind when assessing the rock's durability. The last three columns of Table 1 ("%fraction") show the estimated values for the percentage weight in terms of the content in clayey minerals (CF), insoluble residue (IR) and carbonate content (CB) in the samples we studied. 2% of the weight of AR corresponds to clays while 92% is calcium carbonate, which suggests that this rock is more exposed to damage than MR, which is composed above all of quartz and has a clay fraction of less than 1%. We did not detect organic materials in either rock when we added hydrogen peroxide.

The analysis of the chemical composition via XRF (Table 2) corroborated our findings for mineralogical composition, such that for MR we obtained higher values in the elements related with silicates (above all quartz and feldspars) such as Si, Al and K. The high Fe content is mainly due to the presence of hematite and goethite, while the low Ca and Mg values are due to the presence of calcite and dolomite. In AR, the most notable element is calcium from the calcite. The LOI value is related with carbonate content and is therefore higher in AR than in MR.

The petrological study has shown that MR has a homogenous composition and texture. This rock has a clear clastic texture and the packing is high, in which quartz is the most abundant mineral phase (Figs. 2a, b, and 3a). The quartz clasts are generally sub-rounded to rounded in shape. Some are irregular or oblong varying in size from 20 or 30 μm to up to 500 μm, but with a predominant value around 100–200 μm. The quartz is both monocrystalline and polycrystalline and is of both metamorphic and igneous origin (Clementson Lope et al., 2009). Feldspar crystals were observed in smaller concentrations, above all potassium feldspar with a large proportion of orthoclase and smaller amounts of microcline. We also identified plagioclase crystals with polysynthetic crystal twinning, although in very small proportions compared to the potassium feldspars (Fig. 2c and d, indicated with a red arrow). In many feldspars we observed incipient alteration, in some cases showing significant argillification (Figs. 2d and 3b, white arrows). The secondary mineralogy is varied and the proportion of each of the different phases varies slightly from one sample to the next. The micas are the most abundant of the different phases detected, noting above all the presence of muscovite in long laminar crystals laid out in the same direction as the lamination of the rock (Fig. 2a and b). In some muscovite crystals we detected the presence of fan edges or crystals that had been deformed due to mechanical compactation (Henares et al., 2014) and an alteration to clay. We also observed biotite, although in very small proportions and always associated with crystals that are larger than the muscovite crystals. In many cases, the biotite crystals are altered to chlorite and/or iron oxyhydroxides. We also observed some crystals of dolomite, although it was generally very small which in many cases made them difficult to detect. The dolomite crystals have a skeletal habit (Fig. 3c, red arrow) and their composition was confirmed by EDX microanalysis. We also detected the following accessory phases: opaques, chalcedony (Fig. 2e and f, red arrow), apatite, tourmaline and zircons.

Fig. 2. POM microphotographs showing the main characteristics of the rock fabric of Molinaza Roja (a–f) and Arenisca Ronda (g–l) with and without crosses nichols respectively. "a and b" show the general appearance on MR of the oriented texture of the clasts and dark beds rich in Fe oxides; in "c and d" we can identify a plagioclase crystal (red arrow) and various quartz and feldspar (white arrows indicate argillification process) crystals with a ferruginous-clayey cement; in "e and f" there is a detail of the carbonated cement and a chalcedony crystal (red arrow); in "g and h" in AR we show the fabric composed of extra- and intraclasts, fissures, cement and pores; in "i and j" there is a detail of an extraclast that is rich in fossils and the remains of an intraclast (coral); "k and l" show extraclasts of polycrystalline aggregates of quartz and schists and clay covering the clasts (red arrows). (For interpretation of the references to color in this figure legend, the reader is referred to the web version of this article.)

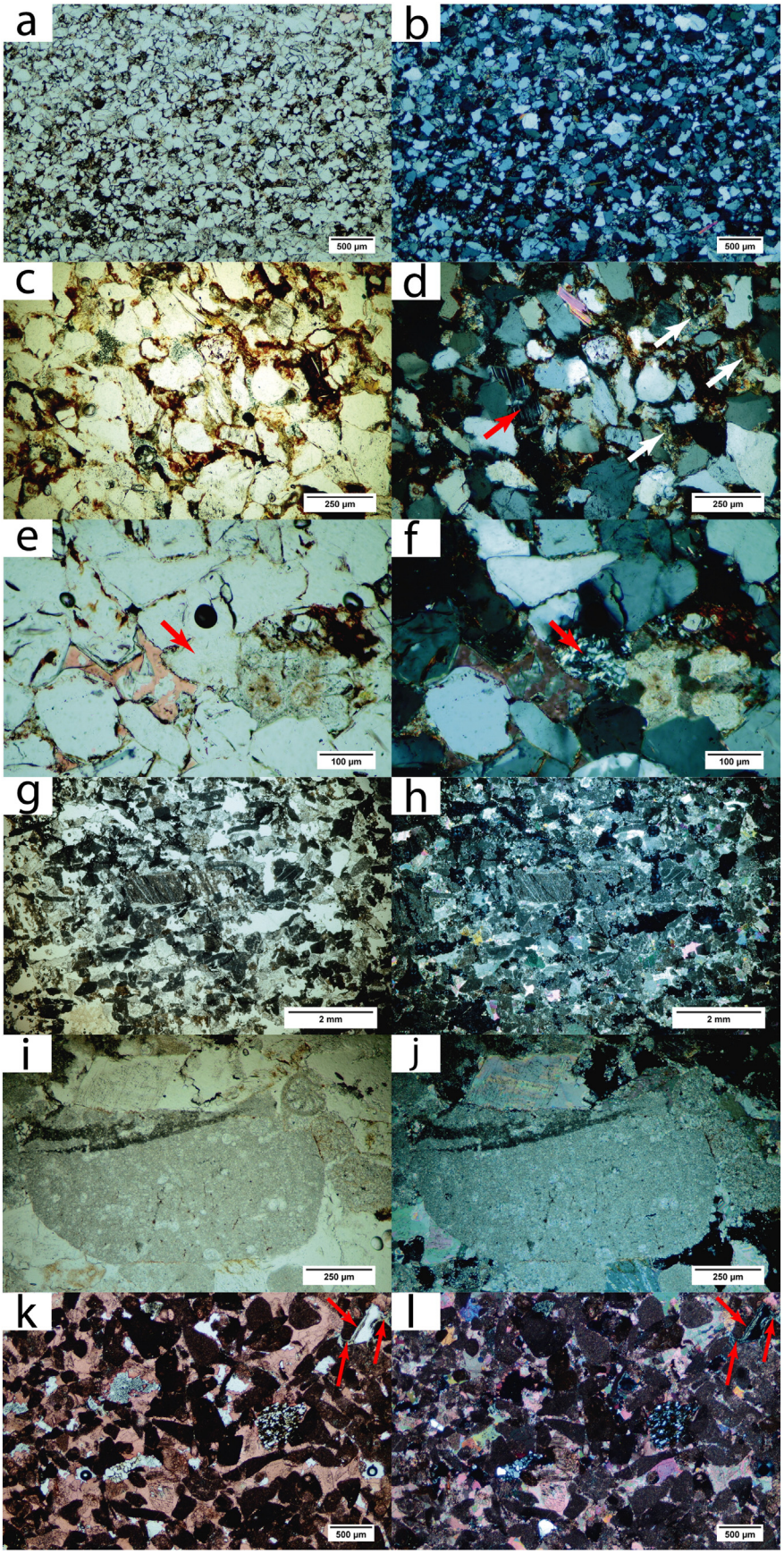
a
500 μm
b
500 μm
c
250 μm
d
250 μm
e
100 μm
f
100 μm
g
2 mm
h
2 mm
i
250 μm
j
250 μm
k
500 μm
l
500 μm

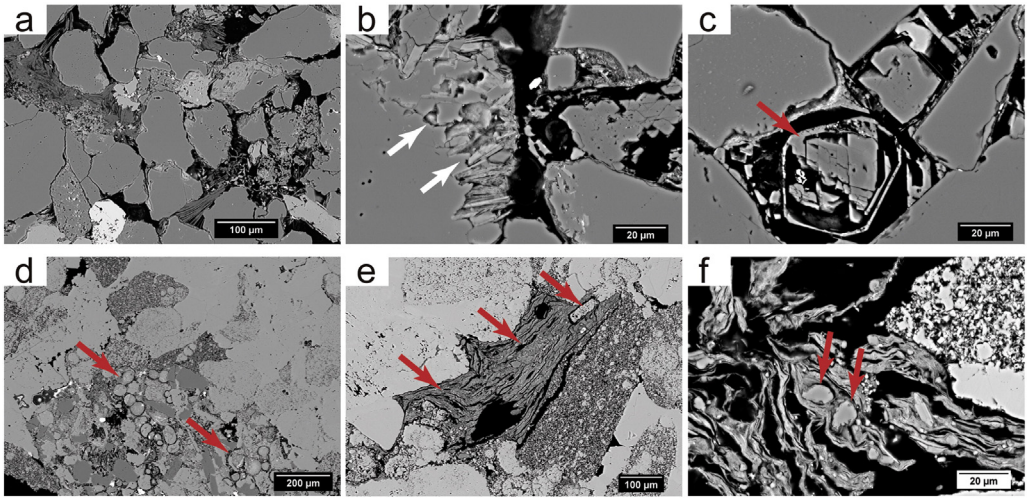

Fig. 3. FESEM images of microtexture of Molinaza Roja (a) and Arenisca Ronda (d) samples, clayification of the potassic feldspar (c, white arrows), dolomite with skeletal habit (d, red arrow), clay aggregates between the carbonated clasts (e, red arrows) and area of weakness due to the presence of clay with encompassed carbonated clasts (f, red arrows). (For interpretation of the references to color in this figure legend, the reader is referred to the web version of this article.)

We identified three types of cement: ferruginous, calcareous and siliceous. These cements offer varying degrees of resistance making the rock more or less durable. The rock's red color comes mainly from the ferruginous cement, which is composed above all of hematites and goethite. We observed that this kind of cement can concentrate in very fine beds (Fig. 2a and b) oriented according to the main lamination of the rock. Together with the areas rich in clay matrix, these beds are what favor the appearance of this lamination. However, in some cases the clay minerals are the result of feldspar alteration which means that they have an authigenic origin and can therefore be considered as an epimatrix. The carbonated cement (Fig. 2e and f) was detected due to the high birefringence of its crystals and after staining the thin sections with alizarin. The most frequently observed cement texture was poikilotopic. In some cases we also observed that the siliceous cement is in syntaxial growth with the quartz crystals. The cements appear as pore or crack fillers, and as fine films around the clasts, especially the clay matrix and the ferruginous cement (Fig. 4a); for this reason, in those samples in which clay matrix is identified, the rock will probably have worse mechanical properties. The pores are difficult to distinguish in that they are small (between 10 and 40 μm) and there are very few of them. According to Pettijohn (1975), this rock can be classified as arkose, with certain tendencies to graywacke depending on the quantity of matrix.

The clasts in the AR sample are composed of carbonates. The clasts are irregular in shape ranging from oblong to subrounded and the size varies from 100 μm to 1 mm, even bigger than 2 mm. The subrounded shape is due to the fact that the clasts have undergone a process of reworking (extraclasts) (Fig. 2g and h). This is because these clasts are rich in matrix, incompatible with the energy of the medium that generated the calcarenite; in some cases they have suffered recrystallization characterized by the presence of microsparite and less frequently pseudosparite. The fossil remains can only be found within the micritic clasts composed above all of foraminifera and gastropods. We also detected the presence of cocolites in the micritic clasts when observing them under the ESEM. Only the large ones (fragments of mollusk valves, fragments of red algae and bryozoa) appear without being associated with micritic clasts (Fig. 2g, h, i, j and 3d). These fossils are also recrystallized in some cases appearing as ghosts. The rounding rate of the micritic clasts indicates the reworking of the original sediment and the presence of cocolites indicates a pelagic carbonatic clay. The cement is very abundant and in some cases two cementation phases can be distinguished. The first phase of cementation consolidates the calcarenite,

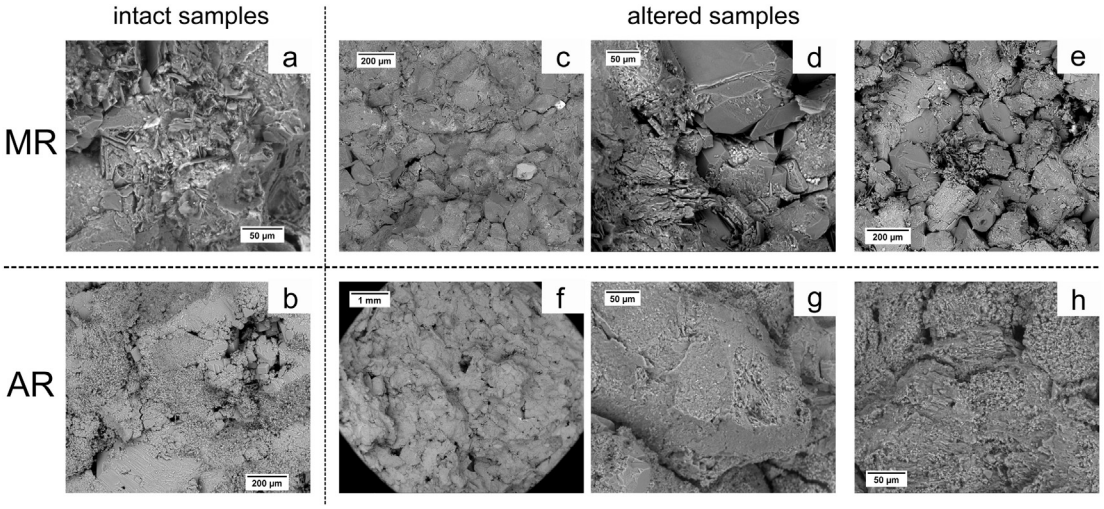

Fig. 4. ESEM images of intact samples (Molinaza Roja (a) and Arenisca Ronda (b)) and samples altered by ice (c, d, f and g) and salt (e and h) crystallization.

Table 3
Characterization of porous system of Molinaza Roja (MR) and Arenisca Ronda (AR). Data obtained by mercury intrusion porosimetry (MIP), nitrogen adsorption (N_2), helium pycnometry (He) and hydric tests (HT). Legend: P_{MIP} and P_{HT}: open porosity (%); ρ_b and ρ_{Hb}: apparent density (kg × m^{-3}); ρ_{sk} and ρ_{Hsk}: skeletal density (kg × m^{-3}); SSA: specific surface area (m^2 × g^{-1}); ρ_{bT}: dry bulk density (kg × m^{-3}); ρ_T: true density (kg × m^{-3}); P_T: total porosity (%); P_C: close porosity (%); A_b: free water absorption (%); A_f: forced water absorption (%); A_x: degree of pore interconnection (%); Di: drying index; S: saturation coefficient (%); C_C: capillarity coefficient (g/m^2 × s$^{0.5}$); H_C: capillarity height (mm × s$^{-0.5}$); c1 and c2: perpendicular and parallel samples orientation to capillary flow; K_v: vapor permeability coefficient (g/m^2 × 24 h). The standard deviation (σ) is indicated in brackets.

	MIP			N_2	He				HT													
	P_{MIP} (σ)	ρ_b	ρ_{sk}	SSA	ρ_{bT}	ρ_T	P_T	P_C	P_{HT} (σ)	P_{Hb}	P_{Hsk}	A_b	A_f	D_i	A_x	S	C_{c1}	C_{c2}	H_{c1}	H_{c2}	K_v (σ)
MR	14.3 (1.0)	2188	2560	4.390	2163	2667	18.5 (1.7)	≈4	14.8 (0.2)	2251	2643	5.6	6.6	319	14.7	71.4	21.1	36.0	0.22	0.37	88 (1)
AR	17.5 (0.2)	2173	2632	5.387	2204	2704	18.9 (0.9)	≈1.5	16.8 (0.1)	2198	2640	7.2	7.6	234	5.4	86.4	27.4	39.0	0.22	0.27	74 (14)

which is deposited in the gaps between the clasts, also producing the recrystallization of the micrite and of the fossils. A second phase of cementation occurred after cracks appeared and then were filled. We also detected syntaxial growth on crystals of sparite and cement in mosaic and poikilotopic textures. Some edges of the sparite crystals are suturated due to recrystallization, while others are straight due to cementation. We also detected various accessory phases such as opaques, quartz aggregates and phyllosilicates, above all muscovite, from schists of the metamorphic materials from the Internal Zones of the Betic Cordillera. In Fig. 2k and l (marked with red arrows) and in Fig. 3e and 3f, we can clearly see that in some cases the clay minerals cover and even encompass other minerals inside the clay matrix. The pore system is clearly defined and associated with the processes of cementation and recrystallization (and dissolution) suffered by this calcarenite. The pores are irregular in shape and associated with the gaps that have not been filled with sparite. There are few interclastic pores and some are mold-like. We also observed that in some cases the porosity is associated with clay-rich areas, which decay easily and result in a loss of material (Fig. 3e), and which on some occasions may create small cracks (Fig. 4b). According to Folk (1959), this rock could be classified as calcarenite.

4.1.2. Pore system and hydric behavior

The results of the porometric, hydric, nitrogen absorption and He pycnometry tests for the two types of rock are summarized in Tables 3 and 4 and in Fig. 5.

The open porosity in MR is 14.3%, while that of AR is 17.5%. The porosity values obtained from hydric tests (P_{HT}) are very similar to those obtained with MIP (P_{MIP}, Table 3).

In AR, the values for total porosity (P_T) obtained using helium pycnometry are very similar to those for open porosity, which means that the closed porosity (P_C) calculated by the difference between the two values is low with a value of around 1.5%. In MR the P_C value is higher than AR at around 4%.

In Table 6, we divided the porosity values of the intact samples (I) into five ranges (<0.1, 0.1–1, 1–10, 10–100, and > 100 μm), obtained from the porosimetric curves in Fig. 5 (continuous line). In a combined view of Fig. 5 and of the porosity values distributed in ranges in Table 6, AR shows a clear bimodal distribution. Approximately 30% of the pores are located in the 1–10 μm range and another more abundant family of pores in the 0.1–1 μm range, with a value of 62%. This high concentration of pores in this second range may be a risk in terms of the durability of AR due to the fact that salt crystallization causes most damage in this pore range (Rodriguez-Navarro and Doehne, 1999). In the case of MR, the distribution is more heterogeneous, with 60% of the pores in the 1–10 μm range. 24% of the pores are in the 0.1–1 μm range, which means that the possible damage due to salt crystallization is undoubtedly much lower. In addition, these values are percentages of the total porosity of the rock and P_{MIP} is lower in MR than in AR. In the part of the porosimetric curve corresponding to the nitrogen absorption analysis (discontinuous curve), both rocks show a maximum around 26 Å.

The highest real density values (ρ_{sk} and ρ_{Hsk}) were measured in AR. In spite of the fact that for the dominant phases in both rocks, quartz in MR and calcite in AR, the real density value is a long way from the theoretical value (2650 kg × m^{-3} for quartz and 2710 kg × m^{-3} for calcite). This is because it is influenced by the other secondary phases, referred to above in the mineralogy section. This difference is greater in AR as it is more porous than MR. The helium pycnometry value is however almost the same as the theoretical values.

The higher specific surface area (SSA) value in AR is due to its higher percentage of clay (CF, Table 1).

The A_b and A_f coefficients (Table 3) obtained from the hydric tests show that AR has a greater water absorption capacity, with a value of 7.2% for absorption at atmospheric pressure and 7.6% in a vacuum. Although the MR values are slightly lower, the interconnection between the pores is worse in MR, as manifested by its higher pore interconnection coefficient (A_x), which means that it is more difficult for liquids to enter and leave the pore system. This may influence the durability of MR in that the salts dissolved in the fluids are more easily retained inside it (Esbert et al., 1997). The absorption capacity of each rock and its degree of interconnection influence their capacity to contain water, such that AR has a saturation coefficient (S, Table 3) of 86.4%, indicating that its empty space is almost saturated in just 48 h. Fig. 6a shows the behavior of each variety and we have shortened the time axis for better visualization of the results. As regards the desorption rate (Di), MR took longer to dry, a logical result given that the interconnection between its pores is worse.

AR shows higher capillarity coefficient values (C_c, Table 3). However the difference found on the basis of the orientation of the samples (C_{c1} and C_{c2}) was lower than that obtained in MR. It is important to point

Table 4
Mercury intrusion porosimetry values for Molinaza Roja (MR) and Arenisca Ronda (AR). Legend: open porosity (P, in %) values and their standard deviation for the three measurements are shown in brackets, bulk density (ρ_b, in kg/m^3), skeletal density (ρ_a, in kg/m^3), partial porosity (P_P, in %), the values in square brackets indicate the amount of relative porosity (in %) and the mean pore size radius (r, in μm) according to pore size ranges (<0.1, 0.1–1, 1–10, 10–100, >100 μm) of intact samples (I) and samples altered in the freeze–thaw (FT) and salt crystallization (Sa) tests.

		P	ρ_b	ρ_a	<0.1		0.1–1		1–10		10–100		>100	
					P_P	r	P_P	r	P_P	r	P_P	r	P_P	r
MR	I	14.3 (1.0)	2217	2586	1.0 [7.0]	0.05	3.4 [24.1]	0.49	8.6 [60.0]	3.76	0.9 [6.6]	33.25	0.3 [2.3]	200.73
	FT	12.6 (0.8)	2294	2527	1.7 [13.1]	0.04	6.9 [58.3]	0.43	2.7 [21.9]	2.72	0.9 [5.6]	39.11	0.4 [1.1]	142.69
	Sa	10.3 (2.4)	2257	2476	1.4 [12.4]	0.04	3.9 [41.2]	0.48	2.6 [26.6]	2.20	1.7 [16.3]	32.35	0.6 [3.6]	194.15
AR	I	17.6 (0.2)	2195	2662	0.5 [3.1]	0.07	10.9 [62.2]	0.46	5.1 [29.3]	2.52	0.7 [4.0]	38.12	0.3 [1.5]	220.61
	FT	16.9 (0.4)	2106	2534	1.2 [6.9]	0.06	12.0 [71.0]	0.36	2.8 [16.7]	2.98	0.8 [4.7]	37.90	0.1 [0.8]	142.28
	Sa	17.5 (0.5)	2220	2695	0.4 [2.4]	0.07	10.1 [57.4]	0.48	5.7 [32.6]	2.71	0.9 [5.1]	43.05	0.4 [2.6]	203.71

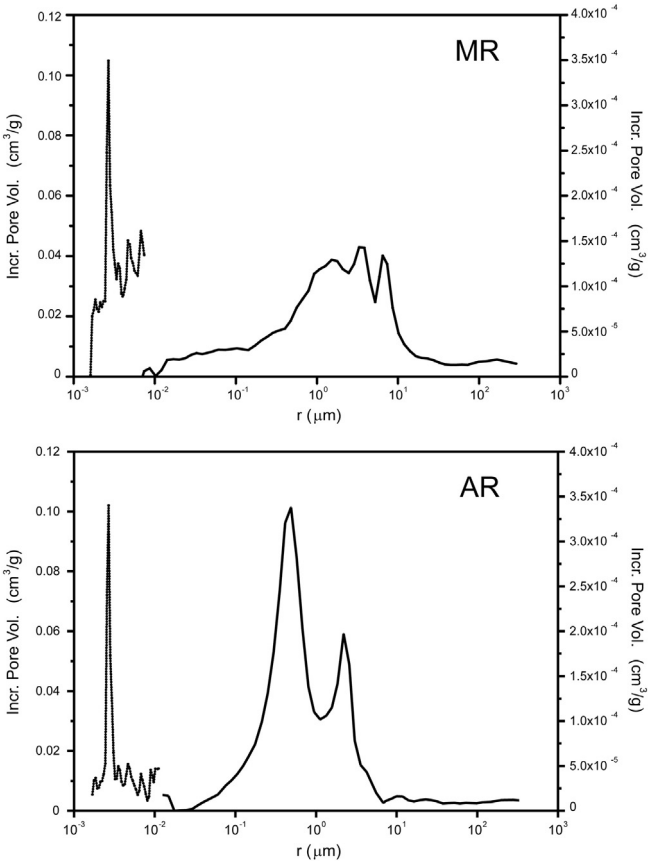

Fig. 5. MIP (continuous line) and BJH (dotted line) pore-size distribution curves for Molinaza Roja (MR) and Arenisca Ronda (AR) stones. Pore radius (in μm) versus Incremental Pore Volume (in cm^3/g) (the left column refers to MIP and the right to BJH analyses). Each curve shows the average of six measures per lithotype.

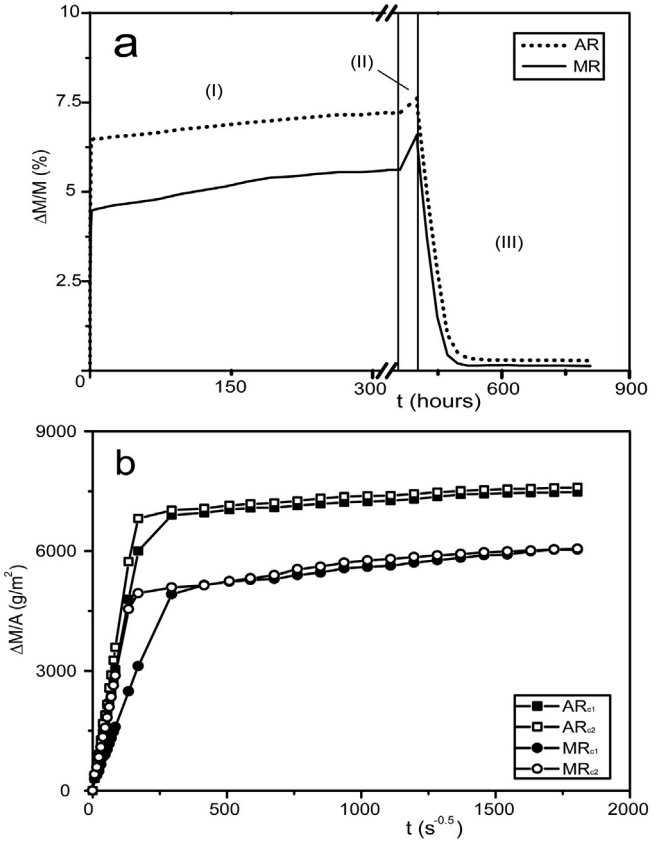

Fig. 6. (a) Free (I) and forced (II) water absorption and desorption (III) curves. (b) The capillarity curves for the different directions c1 (perpendicular) and c2 (parallel).

out that the lay-out of the samples which are orientated parallel to the water rise that facilitates the capillary processes in both rocks, especially in MR (Fig. 6b). This was demonstrated in the capillary velocity and again when the samples were oriented in parallel (H_{c2}) when higher values were obtained than in the c1 direction. It is interesting to note that in the c1 direction, both varieties of rock obtained the same H value, which implies that the capillarity velocity in AR is higher in that direction than in MR because in the same period of time a higher amount of water manages to ascend; by contrast, when the orientation is parallel, MR has a higher H value, which suggests that this rock has a significant capillary suction capacity (see Fig. 6b). Nonetheless in the samples oriented in c2 direction, the tendency to saturation was reached after about 6–8 h; whereas when oriented in the c1 direction, this process was much slower, taking almost 24 h to saturate.

Finally, we measured the permeability to water vapor (K_v, Table 3) of both lithotypes. Although the average value obtained was higher in MR than in AR, which indicates that the first has a greater capacity for transmissibility, in general the two rocks showed very similar values, with K_v equal to 88 and 74 $g/m^2 \times 24$ h, respectively. However if we observe the standard deviation value, AR has more heterogeneous hydric behavior than MR.

4.1.3. Dynamics and mechanical properties

The propagation velocity of the ultrasound waves is higher in AR than in MR (V_p and V_s, Table 5). This difference is due to the mineralogy of each rock, which in the case of AR is composed above all of calcite, while feldspars and above all quartz dominate in MR. This is because calcite propagates the waves more quickly (approx. 6660 m/s) than quartz (approx. 5800 m/s) (Carmichel, 1989). It is clear that the V_p values measured in the rocks are lower than those of these mineral phases taken individually, due to the presence of other minor mineral phases (feldspars, clay minerals, etc.), which together with the textural factors (crystal size, crystal edges, porosity, laminations, preferential orientations, etc.) lead to a fall in velocity (Martínez-Martínez, 2008). This can be seen clearly if we observe the V_p values in the three spatial directions (V_{p1}, V_{p2} and V_{p3}, Table 5). We can also see that in the propagation direction perpendicularly to the lamination, the velocity of V_{p1} is quite a lot lower than in the other two directions. This occurs in both samples, which means that in AR even though in some cases, no preferential orientation can be visually observed, ultrasounds show some discontinuity. This result confirms what we suspected after the capillarity test and the possible influence of the orientation of the rocks on their hydric behavior and the strong influence of the fabric on these properties. The relative anisotropy coefficient (Δm_p) and especially, the total anisotropy coefficient (ΔM_p) confirm the textural heterogeneity of the two rocks. The ΔM_p value is indeed higher in MR than in AR because the lamination is much more pronounced than the orientation of the clasts. In MR it is also necessary to take into account the existence of fine levels that are rich in clay and oxyhydroxides that influence the wave propagation velocity, especially in this direction. The mineral composition has also influenced the Poisson coefficient with MR obtaining a lower value than AR due to the presence of quartz and feldspar compared to calcite (Ji et al., 2009). The other coefficients (E, G and K) indicate that AR has better physical-mechanical behavior than MR.

For a more detailed study of the mechanical properties of the two varieties of rock, we performed uniaxial compression (R_c) and flexural (R_{tf}) tests, the results of which are set out in Table 5. In the case of uniaxial compression, MR shows a much higher resistance value than AR, in both perpendicular and parallel orientations (Rc_{per} is 80 MPa compared to 32 MPa and Rc_{pall} is 74 MPa compared to 35 MPa respectively). This is due to the presence of siliceous and ferruginous cement in MR, which

Table 5
Ultrasonic waves velocities of Molinaza Roja (MR) and Arenisca Ronda (AR) stones. Legend: P- and S-wave velocity values (V_p and V_s, in m/s), P-wave velocity values in the three orthogonal directions (V_{p1}, V_{p2} and V_{p3}, in m/s), relative (Δm_p) and total (ΔM_p) anisotropy coefficients of P-waves, Poisson coefficient (ν),Young module (E, in GPa), shear module (G, in GPa), volume module (K, in GPa), P-wave velocity values after freeze–thaw (V_{pFT}) and salt crystallization (V_{pSa}) tests, compressive strength perpendicular ($R_{c\ per}$, in MPa) and parallel ($R_{c\ pall}$, in MPa) to the charge load and flexural strength (R_F, in MPa). The standard deviation of the measurements is shown in brackets.

	Dynamics coef.											Statics coef.		
	V_p	V_s	V_{p1}	V_{p2}	V_{p3}	Δm_p	ΔM_p	ν	E	G	K	$R_{c\ per}$	$R_{c\ pall}$	R_{tf}
MR	3286	2254	2897	3530	3432	5.5	16.8	0.15	23.6	10.7	10.2	80	74	7.5
	(403)	(206)	(163)	(87)	(180)	(4.0)	(3.6)	(0.1)	(4.4)	(2.0)	(4.7)	(1)	(3)	(0.7)
AR	3757	2326	3792	4348	4097	6.0	10.2	0.26	29.9	11.9	20.8	32	35	10.5
	(131)	(126)	(60)	(41)	(90)	(3.1)	(0.9)	(0.03)	(3.2)	(1.3)	(3.6)	(4)	(5)	(0.5)

provide greater resistance than that offered by the carbonated cement in AR. In addition the greater porosity and pore size (Table 2) and the higher percentage of clays (CF, Table 1) in AR also make it less resistant than MR. Various authors (Tamrakar et al., 2007; Sabatakakis et al., 2008; Zorlu et al., 2008) have shown the influence of oriented texture, crystal size, degree of cementation, packing, etc. on the compressive strength. Based on these studies we found that the amount and mineralogical composition of cement as well as the smaller size of grains and higher packing in MR compare to AR cause an increase in compressive strength. Furthermore, according to Sabatakakis et al. (2008), the lower resistance of AR is partially due to the size of calcite crystals (sparite or micrite) and their amount, because the grain size of sparitic textures is greater and the degree of packing is less dense, which would cause a lower R_c value. On the other hand, when the load was laid parallel to the lamination, the resistance of MR fell, albeit not sharply, when compared to when the load was laid perpendicular to it; in AR the resistance value was practically the same regardless of the orientation on the basis of its textural anisotropy. In this case, we can observe how the lamination in MR was more decisive than the crystal size or cementation. The R_c results contradict the findings of the ultrasound analysis described in the previous paragraph, in which AR showed better mechanical behavior. This suggests that in this case the ultrasound measurement has been less effective in estimating the mechanical properties compared to the compression test. This is because of the important role of the rock fabric especially (lower crystal size and strong lamination in MR than AR) and the composition of these two varieties. With regard to the results of the flexural test, AR obtained slightly higher values than MR, with 10.5 MPa compared to 7.5 MPa, respectively.

4.1.4. Color measurement

Table 6 shows the chromatic values for each rock (I, Table 6). In both rocks the values of the chromatic axes, a* and b*, tend towards values of red and yellow, with the tendency towards axis b* dominating. The higher a* value for MR is due to the presence of Fe oxyhydroxides. As regards L*, as AR has a lighter color (due to the presence of calcite in both the cement and the clasts), it has a higher L* value than MR, at 72.5 and 56.5, respectively. The standard deviation shows a low dispersion of average values, although as the maximum and minimum values indicate that (max–min, Table 6), there are some samples with values that are quite a lot higher or lower than the average. In general, the values indicate that, due to its texture, AR is more heterogeneous than MR, which leads to a more pronounced variation in color.

Table 6
Color measurements for intact (I) and altered samples after freeze–thaw (FT) and salt crystallization (Sa) tests. Legend: L*: lightness; a* and b*: chromatic parameters; ΔE^*_{94}: Color differences between intact and altered samples; Φ (σ): mean value of L*, a*, b* of intact samples and the standard deviation are shown in brackets; Max–min: the maximum and minimum values measured in intact stones; FT (σ) and Sa (σ): are the values measured in the freeze–thaw and salt test, respectively and their standard deviation. For stone acronyms see Table 1.

			L*		a*		b*		ΔE^*_{94}
MR	I	Φ (σ)	56.5	(1.8)	10.1	(0.5)	14.7	(0.8)	–
		Max–min	69.4	48.7	12.8	9.2	17.6	12.5	
	FT (σ)		58.3	(4.4)	9.8	(1.2)	15.1	(2.9)	1.9
	Sa (σ)		59.1	(2.4)	10.6	(1.8)	15.5	(1.6)	2.8
AR	I	Φ (σ)	72.5	(3.6)	5.9	(1.6)	16.8	(4.2)	–
		Max–min	77.8	59.4	7.4	3.3	25.3	10.3	
	FT (σ)		72.5	(4.6)	5.9	(2.8)	17.8	(5.8)	1.0
	Sa (σ)		72.4	(4.8)	5.9	(2.9)	20.5	(5.8)	3.7

4.2. Comparison of altered and intact stones

4.2.1. Accelerated decay test

The results of the salt crystallization and freeze–thaw resistance tests are shown in Fig. 7.

The salt-crystallization test had very damaging effects on AR (Fig. 7a, empty markers), which lost over 40% of its initial weight. It is interesting to note that this damage occurred in three stages. In the first stage (up until the 2nd cycle), the porous system was saturated with salt solution; in stage two, from the 3rd and 4th cycle onwards, fragments began to fall off the samples. This decay continued until it reached minimum levels in Cycle 10, by which time the sample had already lost a substantial amount of material. In these cycles the decay took the form of spalling on planes parallel to the preferential orientation of the clasts and the loss of small fragments. This form of decay could be defined as delamination or even exfoliation and sanding (Vergès-Belmin, 2008). From Cycle 11 the loss of material resumed (Stage Three) and continued until the end of the test. This further decay was due to new salt solution getting into the fissures that had developed between the sedimentary planes, so producing an increase in salt crystallization pressure. Anania et al. (2012) observed a similar behavior in their samples and in particularly with AR. The measurement of ultrasounds every five cycles enabled us to record these changes thanks to the variation in the P-wave velocities as we progressed through the aging test cycles. As a result in Fig. 7b (AR_{Sa}) we observed that in Cycle 5 there was a reduction in V_P due to the appearance of fissures and a small delamination and decohesion of grains on the surface. In Cycle 10, the fact that these fissures were now full of salt caused an increase in V_p; the samples suffered another loss of material that was so serious that it prevented us from making the last ultrasound measurement. In MR by contrast, although there was no large loss of materials, there was a slight sanding on the surface due to the fact that the mirabilite–thenardite transformation took place near the surface (Benavente et al., 2004; Espinosa et al., 2001). The ultrasound results in Fig. 7b (MR_{Sa}) show an increase in the P-wave velocity up to the last reading when a slight fall occurred. This may be interpreted as the progressive filling of the pores with salt solution. The fall in velocity in the final reading indicates that fissures have appeared parallel to the lamination which may result in loss of material. Therefore, the trend in the variation of V_p due to the loss of grains on the sample surface and the appearance of fissures, was mainly due to the rock fabric and its behavior through the action of salts crystallization, with a strong influence of porosity.

The freeze–thaw test did not cause any visible damage and there were no changes in the weight of the samples (Fig. 7a and Table 6). However, the ultrasound reading shows that the rocks did suffer fatigue (Fig. 7b), with a fall in V_p, especially from Cycle 10 onwards. As happened in MR with the salt crystallization test, this fall is probably the

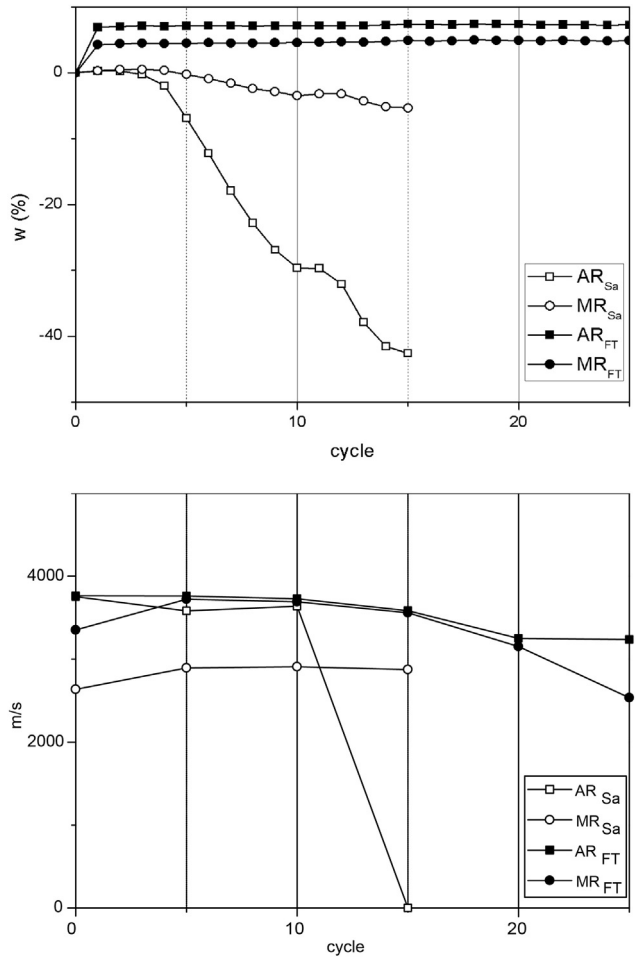

Fig. 7. Weight loss evolution (a) and ultrasound velocity variation (b) of Molinaza Roja (MR) and Arenisca Ronda (AR) when subjected to the salt crystallization test (open symbols) and freeze–thaw test (close symbols).

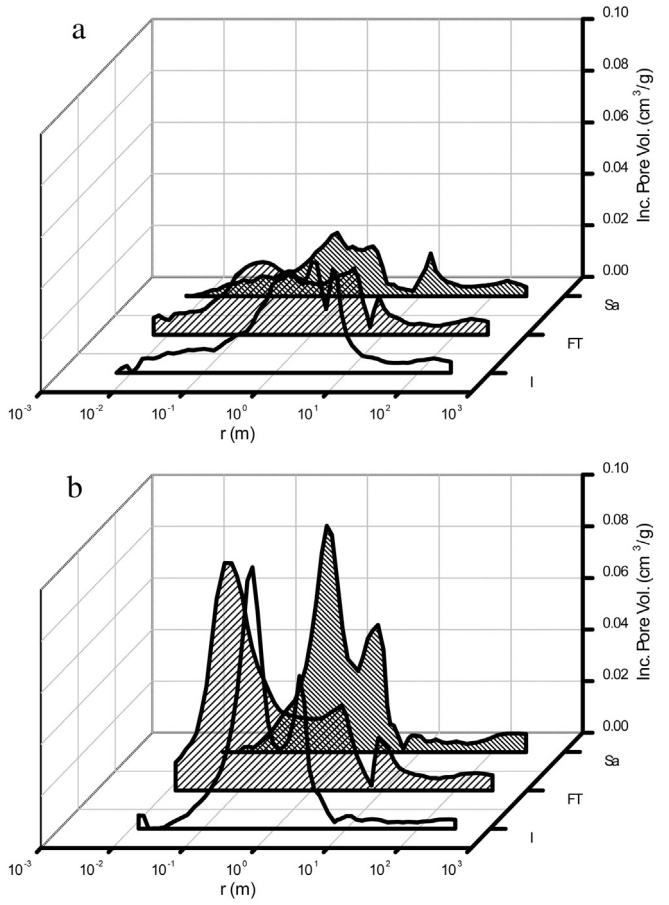

Fig. 8. Pore size distribution curves for intact (I) and altered specimens after freeze–thaw (FT) and salt crystallization (Sa) tests on Molinaza Roja (MR) and Arenisca Ronda (AR). Pore entry radius (in μm) versus incremental pore volume (in cm^3/g).

result of the appearance of small cracks that cannot be seen with the naked eye. In fact when we finished the test, one of the MR samples broke in half along the lamination surface.

4.2.2. Evaluating the decay effects on porous system

The ability to identify the changes in the porous system is of great importance due to the fact that the intrinsic properties of each rock and the characteristics of each aging test feed off each other to increase the decay in the samples.

We assessed the changes in the porous system using MIP. The results for the altered samples are set out in Table 4 and in Fig. 8. In the case of MR, we can see that the porosity value (P_{MIP}, Table 4) has fallen slightly after the accelerated aging test, while in AR the percentage has remained practically unchanged. If we begin by looking at the results for the freeze–thaw test, the fall in MR may be due above all to the variability of the porosity in this lithotype. We should however note the drop in the 1–10 μm range, while the percentage of pores in the <0.1 μm and 0.1–1 μm ranges has increased. This variation in the pore system in MR was very similar after the salt crystallization test although less dramatic compared to the freeze–thaw test. A similar process took place in the AR samples as regards certain variations in the aforementioned ranges. In addition in both rocks, the absence of large pores may have been one of the factors that made them more resistant to freeze–thaw damage, as ice damage tends to focus on this kind of pore (Everett, 1961). It is also important to bear in mind that these samples have a substantial percentage of cement, which makes them more resistant to alteration by external agents when compared with other rocks with similar characteristics (Molina et al., 2013). For this reason, in spite of having a high saturation coefficient (S, Table 3) the cohesion between the clasts provided by the cement was sufficient to ensure that there was practically no decay.

As commented earlier, the salt crystallization test caused most damage to the samples, especially AR (Fig. 7). The damage suffered by AR happened above all due to the characteristics of its porous system and of the presence of swellable clays. The role of the porous system in the damage was due to the large number of pores in the 0.1–1 μm range (Table 4). Previous authors found that the pressure exerted by the salts when they crystallize inside the pores is at a maximum in this range (Everett, 1961). For this reason the damage was greater than in MR. In fact the percentage of pores in this range increased, which must have exacerbated the decay as the test went on. In addition to the fatigue processes due to changes associated with expandability-contraction of the swellable clays, we have to add the effect of salt crystallization in the first millimeters (Benavente et al., 2004; Espinosa et al., 2001). In MR, the percentage of porosity for the ranges <0.1 μm, 0.1–1 μm and 10–100 μm increases compared to the intact samples. The variation in these ranges is due to the fact that the pores in the 1–10 μm range are filled with salt, causing their percentage to fall and new fissures to appear in the ranges greater than 10 μm. These results enable us to confirm the variation noted with ultrasounds, which was related with an incipient loss of cohesion between the clasts or in favor of lamination.

4.2.3. Changes in the rock fabric of the altered stones

The study of the changes in the fabric of the samples that were altered in the two accelerated aging tests can be seen in Fig. 4. As

mentioned above, the freeze–thaw test did not cause alterations that were visible to the naked eye. However in MR we detected the presence of small fissures (Fig. 4c) and the loss of cementing material (Fig. 4d) between the clasts. This loss of cement caused the layers to separate in the phyllosilicates, facilitating the break-up of the clasts. At a small scale these phenomena confirm the decay that the rock could undergo. The changes in AR were more difficult to detect. Fissures could be observed in the altered samples (Fig. 4f), although they were also visible in intact samples (Fig. 4b), making it difficult for us to establish whether they had appeared as a result of the effect of ice crystallization. One clue was that the fissures in the altered samples were bigger than those observed in the healthy samples. However, some calcite crystals showed serious alteration on the surface and fracturing (Fig. 4g).

The damage caused by the salt crystallization test was much more evident. In MR (Fig. 4e) we observed, as happened in the freeze–thaw test, an important loss of cementing material and an increase in the separation according to the basal planes of the phyllosilicates. We did not observe the appearance of fissures so clearly but we did detect serious fracturing in some quartz and feldspar crystals. In AR, the damage was mainly due to the appearance of new fissures running parallel to the orientation of the clasts, in some cases exacerbated by the presence of clays between the micrite (Fig. 4h). In this case the fissures were produced by the pressure caused by salt crystallization. We also observed the appearance of small fissures with no preferential orientation in the micrite clasts. Both cases of fissuring are responsible for the intense loss of material suffered by AR during the salt crystallization test. We also again observed that the large calcite crystals appeared fractured.

Lastly, the changes brought about by the accelerated aging tests had no effect on the color of the samples compared to the intact ones (Table 6). The only difference we detected was between the AR samples damaged by the salt crystallization test and the intact samples, with a ΔE value of 3.6. However the values for the damaged samples are within the color variability range typically presented by AR, which means that this variation is more due to the heterogeneity of this rock than to the action of the aging tests.

5. Conclusions

We performed a petrological and petrophysical characterization of two varieties of natural stone, Molinaza Roja (MR) quarried in Montoro and Arenisca Ronda (AR) from Ronda (southern Spain). On the basis of the results obtained we came to the following conclusions.

The Molinaza Roja rock variety was classified as an arkose and in terms of mineral composition it is made up mainly of quartz with secondary phases of feldspars and muscovite. We also detected a small clay fraction made up mainly of illite and kaolinite. The rock's characteristic reddish color comes from its iron oxyhydroxides which are often concentrated in fine beds running parallel to the main lamination. We determined the presence of four kinds of cement (siliceous, ferruginous, clay and carbonated). The texture is strongly laminated, which proved a crucial factor in its hydric behavior, especially depending on the direction in which the lamination is orientated and in the propagation of ultrasound waves. The rock shows good mechanical behavior and no differences were observed when the orientation of the samples was changed. The porous system is less clearly defined than in Arenisca Ronda, with most pores being concentrated in the 1–10 μm range and the pore interconnections are worse. Of the two accelerated aging tests we performed, the salt crystallization test had the greatest impact on the durability of the rock. Our observations of the changes in the texture after the two aging tests showed that the rock had lost a substantial amount of cement, which means that in this rock there is important decay in the form of sanding. We also observed the appearance of small fissures, especially after the freeze–thaw test. This fact was confirmed by ultrasounds, which registered a fall in the P-wave propagation velocity. As regards color, no differences were observed between the intact and the altered samples.

Arenisca Ronda is a calcarenite composed of fossilized skeletal fragments and subrounded micrite clasts. The rock has undergone numerous processes of cementation and recrystallization, which have had decisive effects above all on the configuration of the porous system. A substantial amount of clay (around 2%), composed above all of smectite, was detected in this variety of rock. The percentage of porosity was somewhat higher than in Molinaza Roja, at around 17.5%, but it is better connected. As regards the pore size distribution, it has a high percentage in the 0.1–1 μm range. In terms of hydric behavior, it showed a higher water saturation capacity and saturation took place more quickly, but it was also effective in terms of desorption processes in comparison with Molinaza Roja. The propagation of ultrasound waves was strongly influenced by the rock fabric and in some cases a preferential orientation of the clasts could be detected. Resistance to compression was lower compared to the other variety of rock but flexural resistance was higher. Its behavior during the accelerated aging tests was similar to that of Molinaza Roja. In the freeze–thaw test the rock did not suffer any damage that was visible to the naked eye, whereas the salt crystallization test caused serious damage. This rock decayed more than the other one because it has a high number of pores in the 0.1–1 μm range, where crystallization can exert high levels of pressure and because of the high percentage of smectites. These factors meant that the strain suffered by Arenisca Ronda was worse than in Molinaza Roja, so producing greater decay. The types of decay in this lithotype were above all delaminations and to a lesser extent sanding. No appreciable color changes could be noted between intact and altered samples.

In general the Molinaza Roja rock is more resistant to decay than Arenisca Ronda. Although there are small differences in some of their properties, the most serious problems for the durability of Arenisca Ronda lie in the high number of pores in the 0.1–1 μm range and the presence of smectite. The orientation of textural heterogeneities is also very important as these are weakness planes which, when combined with the different decay agents, facilitate the loss of cohesion between the clasts and the resulting deterioration of the rock. It is therefore recommended that the orientation of these heterogeneities be taken into consideration when laying the stones in new buildings. The presence of moisture and soluble salts can also have negative effects on durability, especially in the case of Arenisca Ronda which is more susceptible to decay.

Acknowledgments

This study was financially supported by Research Group RNM179 of the Junta de Andalucía and by Research Project MAT2012-34473. We are grateful to Nigel Walkington for his assistance in translating the original text.

References

Alonso, F.J., 1986. Caracterización petrofísica y alterabilidad de calizas y dolomías (PhD Thesis), University of Oviedo (209 pp.).
Anania, L., Badalà, A., Barone, G., Belfiore, C.M., Calabrò, C., La Russa, M.F., Mazzoleni, P., Pezzino, A., 2012. The stones in monumental masonry buildings of the "Val di Noto" area: new data on the relationships between petrographic characters and physical–mechanical properties. Constr. Build. Mater. 33, 122–132.
Armengot de Pedro, J., Moreno de Castro, E., Pérez Domínguez, H., Castelló Montori, R., Ramírez Copeiro, J., 1972. Mapa Geológico de España 1:50.000. Hoja 903 Montoro. Instituto Geológico y Minero de España (IGME), Madrid.
ASTM D 2845-05, 2005. Standard method for laboratory determination of pulse velocities and ultrasonic elastic constants of rock. ASTM D2845-05.
Barbera, G., Barone, G., Mazzoleni, P., Scandurra, A., 2012. Laboratory measurement of ultrasound velocity during accelerated aging tests: Implication for the determination of limestone durability. Constr. Build. Mater. 36, 977–983.
Bayram, F., 2012. Predicting mechanical strength loss of natural stones after freeze–thaw in cold regions. Cold Reg. Sci. Technol. 83–84, 98–112.
Bell, F.G., 1993. Durability of carbonate rock as building stone with comments on its preservation. Environ. Geol. 21, 187–200.
Benavente, D., García del Cura, M.A., Garcia-Guinea, J., Sanchez-Moral, S., Ordoñez, S., 2004. Role of pore structure in salt crystallization in unsatured porous stone. J. Cryst. Growth 260, 534–544.
Bruton, G., 1955. Vapour glycolation. Am. Mineral. 40, 124–126.

Cámara, B., De los Ríos, A., García-del-Cura, M.A., Galván, V., Ascaso, C., 2008. Biorreceptividad de las dolomías a la colonización fúngica. Mater. Constr. 58, 113–124.
Cárdenes, V., Monterrosso, C., Rubio, A., Mateos, F.J., Calleja, L., 2012. Effect of freeze–thaw cycles on the bending strength of roofing slate tiles. Eng. Geol. 129–130, 91–97.
Cárdenes, V., Rubio-Ordóñez, A., Monterrosso, C., Mateos, F.J., 2014. Guidelines for selecting roofing slate for the restoration of historical buildings and monuments: two case studies. J. Cult. Herit. 15, 203–208.
Carmichel, R.S., 1989. Practical hanbook of physical properties of rocks and mineral. CRS Press Inc., USA.
Chen, G., Wang, J., 1998. The preparation of marine geological certified reference materials-polymetallic nodule GSPN-1 and marine sediment GSMS-1 from the Central Pacific Ocean. Geostand. Geoanal. Res. 22, 119–125.
Choquette, P., Pray, L.C., 1970. Geologic nomenclature and classification of porosity in sedimentary carbonates. Am. Assoc. Pet. Geol. Bull. 5, 207–250.
Clementson Lope, J.A., 2012. Caracterización de las propiedades de la arenisca de Montoro, sus alteraciones y su aplicabilidad para la construcción (PhD Thesis), University of Cordoba (332 pp.).
Clementson Lope, J.A., Montealegre Contreras, L., Barrios Neira, J., 2007. Tipología de alteraciones en la arenisca roja de Montoro. Macla 7, 86.
Clementson Lope, J.A., Barrios Neira, J., Montealegre Contreras, L., 2009. Determinación de la mineralogía, composición química y textura del material pétreo empleado en los monumentos de Montoro (Córdoba). Macla 11, 59–60.
Cultrone, G., de la Torre, M.J., Sebastián, E., Cazalla, O., 2003. Evaluación de la durabilidad de ladrillos mediante técnicas destructivas (TD) y no-destructivas (TND). Mater. Constr. 53, 41–59.
Cultrone, G., Sebastian, E., Ortega Huertas, M., 2007. Durability of masonry systems: a laboratory study. Constr. Build. Mater. 21, 40–51.
del Olmo Sanz, A., Moreno Serrano, F., Campos Fernández, J., Estévez, A., García-Dueñas, V., García-Rossell, L., Martín Algarra, A., Orozco, A., Sanz de Galdeano, C., 1981. Mapa Geológico de España 1:50.000. Hoja 1051 Ronda. Instituto Geológico y Minero de España (IGME), Madrid.
Dunford, A.M., Parry, A.R., Shipway, P.H., Viner, H.E., 2012. Three-dimensional characterization of surface texture for road stones undergoing simulated traffic wear. Wear 292–293, 188–196.
Dunning, J.D., Huf, W.L., 1983. The effects of aqueous chemical environments on crack and hydraulic fracture propagation and morphologies. J. Geophys. Res. 88, 6491–6499.
Esbert, R.M., Ordaz, J., Alonso, F.J., Montoto, M., González Limón, T., de Buergo, Álvarez, Ballester, M., 1997. Manual de diagnosis y mantenimiento de Materiales pétreos y cerámicos. Collegi d'Apparelladors y Arquitectes Tècnics de Barcelona.
Esbert, R.M., Alonso, F.J., Ordaz, J., 2008. La petrofísica en la interpretación del deterioro y la conservación de la piedra de edificación. Trab. Geol. 28, 87–95.
Espinosa, R.M., Hamilton, A., McNall, M., Whiteker, K., Scherer, G.W., 2001. The chemomechanics of crystallization during rewetting of limestone impregnated with sodium sulphate. J. Mater. Res. 26, 1472–1481.
Espinosa, R.M., Franke, L., Deckelmann, G., 2008. Model for the mechanical stress due to the salt crystallization in porous materials. Constr. Build. Mater. 22, 1350–1367.
Everett, D.M., 1961. The thermodynamics of frost damage to porous solids. Trans. Faraday Soc. 57, 2205–2211.
Fasana, S., Nelva, R., 2013. Improvement of the performance of traditional stone roofs by wind driven rain experimental tests. Constr. Build. Mater. 25, 1491–1502.
Fernández, J., Gil, A., 1989. Interpretación sedimentaria de los materiales triásicos de facies Buntsandstein en las Zonas Externas de las Cordilleras Béticas y en la Cobertera Tabular de las Meseta. España. Rev. Soc. Geol. 2, 113–124.
Folk, R.L., 1959. Practical petrographic classification of limestone. Bull. Am. Assoc. Pet. Geol. 43, 1–38.
Fort, R., 2008. La Piedra Natural y el Patrimonio construido: un mismo campo de investigación. Mater. Constr. 58, 289–290.
Fort, R., 2009. La piedra natural y su presencia en el Patrimonio Histórico. Enseñanzas de las Ciencias de la Tierra 17, pp. 16–25.
Fort, R., Varas, M.J., Alvarez de Buergo, M., Martin-Freire, D., 2011. Determination of anisotropy to enhance the durability of natural stone. J. Geophys. Eng. 8, 132–144.
Franzen, C., 2004. Moisture sorption of natural building stone. In: Kwiatkowski, D., Löfvendahl, R. (Eds.), Proceedings of the 10th International Congress on Deterioration and Conservation of Stone, Sweden, Stockholm, pp. 75–82.
Gibbon, W., Moreno, T. (Eds.), 2002. The Geology of Spain. The Geological Society, London.
González de Vallejo, L.I., Ferrer, M., Ortuño, L., Oteo, C., 2002. In Ingeniería Geológica, editor, Madrid, Pearson Education, 744 pp.
González García, F., Sánchez Camazano, M., 1968. Differentiation of kaolinite from chlorite by treatment with dimethylsulphoxide. Clay Miner. 7, 447–450.
Gregg, S.J., Sing, K.S.W., 1982. Adsorption, surface area and porosity. Academic, London.
Grossi, C.M., Brimblecombe, P., Harris, I., 2007. Predicting long term freeze–thaw risks on Europe built heritage and archaeological sites in a changing climate. Sci. Total Environ. 377, 273–281.
Gutiérrez, J., Mas, A., Gil, E., Galvañ, V., 2012. Clay-related damage in rainscreen walls built with natural stone coverings. Constr. Build. Mater. 29, 357–367.
Guydader, J., Denis, A., 1986. Propagation des ondes dans les roches anisotropes sous contrainte évaluation de la qualité des schistes ardoisiers. Bull. Eng. Geol. 33, 49–55.
Henares, S., Caracciolo, L., Cultrone, G., Fernández, J., Viseras, C., 2014. The role of diagenesis and depositional facies on pore system evolution in a Triassic outcrop analogue (SE Spain). Mar. Pet. Geol. 51, 136–151.
Ji, S., Wang, Q., Salisbury, M.H., 2009. Composition and tectonic evolution of the Chinese continental crust constrained by Poisson's ratio. Tectonophysics 463, 15–30.
Langella, A., 2000. Preliminary contribution on durability of some macroporous monumental stones used in historical towns of Campania region, Southern Italy. 9th International Congress on Deterioration and Conservation of Stone, Venice.
Laycock, E.A., 2002. Ten years of frost testing at Sheffield Hallam University. Constr. Build. Mater. 16, 195–205.
Lombillo, I., Thomas, C., Villegas, L., Fernández-Álvarez, J.P., Norambuena-Contreras, J., 2013. Mechanical characterization of rubble stone masonry walls using non and minor destructive tests. Constr. Build. Mater. 43, 266–277.
Luque Aranda, A., 2010. Andalusian marbles: durability criteria applied in its use as ornamental stone (PhD Thesis), University of Granada (215 pp.).
Martín Ramos, J.D., 2004. XPowder, a software package for powder X-ray diffraction analysis. Lgl. Dep. GR 1001/04.
Martínez-Martínez, J., 2008. Influencia de la alteración sobre las propiedades mecánicas de calizas, dolomías y mármoles. Evaluación mediante estimadores no destructivos (Ultrasonidos) (PhD Thesis), University of Alicante (295 pp.).
Massey, S.W., 1999. The effects of ozone and NO_X on the deterioration of calcareous stone. Sci. Total Environ. 227, 109–121.
McAlister, J.J., Smith, B.J., Török, A., 2006. Element partitioning and potential mobility within surface dusts on buildings in a polluted urban environment, Budapest. Atmos. Environ. 40, 6780–6790.
McAlister, J.J., Smith, B.J., Török, A., 2008. Transition metals and water-soluble ions in deposits on a building and their potential catalysis of stone decay. Atmos. Environ. 42, 7657–7668.
McCabe, S., Smith, B.J., Warke, P.A., 2009. Exploitation of inherited weakness in fire-damaged building sandstone: the 'fatiguing' of 'shocked' stone. Eng. Geol. 115, 217–225.
Miranda, L.F., Rio, J., Miranda Guedes, J., Costa, A., 2012. Sonic impact method — a new technique for characterization of stone masonry walls. Constr. Build. Mater. 36, 27–35.
Molina, E., Cultrone, G., Sebastian, E., 2011a. Descripción petrográfica y química de dos materiales pétreos empleados en el Patrimonio Construido de Andalucía. Macla 15, 133–134.
Molina, E., Cultrone, G., Sebastian, E., Alonso, F.J., Carrizo, L., Gisbert, J., Buj, O., 2011b. The pore system of sedimentary rocks as a key factor in the durability of building materials. Eng. Geol. 118, 110–121.
Molina, E., Cultrone, G., Sebastian, E., Alonso, F.J., 2013. Evaluation of stone durability using a combination of ultrasound, mechanical and accelerated aging tests. J. Geophys. Eng. 10, 035003.
Moore, D.M., Reynolds, R.C., 1989. X-ray diffraction and the identification and analysis of clay minerals. Oxford University Press, Oxford (322 pp.).
Moropoulou, A., Bakolas, A., Bisbikou, K., 2000. Investigation of the technology of historic mortars. J. Cult. Herit. 1, 45–58.
Mulvin, L., Lewis, J.O., 1994. Architectural detailing, weathering and stone Decay. Build. Environ. 29, 113–138.
Niembro Bueno, M.C., 2009. Wavelength dispersive X-ray fluorescence analysis of major and trace elements in marine sediments by the fundamental parameters method: using geochemical proxies for paleoenvironmental reconstruction, unpublished master's thesis, University of Granada.
NORMAL 21/85, 1985. Permeabilità al vapor d'acqua. CNR-ICR, Rome, Italy.
NORMAL 29/88, 1988. Misura dell'indice di asciugamento (drying index). CNR-ICR, Rome, Italy.
Pettijohn, F.J., 1975. Sedimentary rocks. third ed. Harper and Brothers Publisher, New York (618 pp.).
Prieto, B., Silva, B., 2005. Estimation of the potential bioreceptivity of granitic rocks from their intrinsic properties. Int. Biodeterior. Biodegrad. 56, 206–215.
RILEM, 1980. Recommended test to measure the deterioration of stone and to assess the differences of treatment methods. Mater. Struct. 13, 175–253.
Roc Máquina, 2013. La piedra natural de España. Directorio anual de la piedra natural. Reed Business Information, Bilbao (290 pp.).
Rodríguez-Fernández, J., 1982. El Mioceno del sector central de las Cordilleras Béticas (PhD Thesis), University of Granada (224 pp.).
Rodríguez-Gordillo, J., Sáez-Pérez, M.P., 2006. Effects of thermal changes on Macael marble: experimental study. Constr. Build. Mater. 20, 355–365.
Rodriguez-Navarro, C., Doehne, E., 1999. Salt weathering: influence of evaporation rate, supersaturation and crystallization pattern. Earth Surf. Process. Landf. 24, 191–209.
Ruíz-Constán, A., Galindo-Zaldívar, J., Pedrera, A., Sanz de Galdeano, C., 2008. Gravity anomalies and orthogonal box fold development on heterogeneous basement in the Neogene Ronda Depression Western Betic Cordillera. J. Geodyn. 47, 210–217.
Sabatakakis, N., Loukis, G., Tsiambaos, G., Papanakli, S., 2008. Index properties and strength variation controlled by microstructure for sedimentary rocks. Eng. Geol. 97, 80–90.
Scott, V.D., Love, G., 1983. Quantitative electron-probe microanalysis. John Wiley & Sons, Inc., New York.
Serrano, F., 1979. Los foraminíferos planctónicos del Mioceno superior de la cuenca de Ronda y su comparación con los de otras áreas de las Cordilleras Béticas (PhD Thesis), University of Malaga (272 pp.).
Siegesmund, S., Ullermeyer, K., Weiss, T., Tschegg, E.K., 2000. Physical weathering of marbles caused by anisotropic thermal expansion. Int. J. Earth Sci. 89, 170–182.
Simmons, G., 1965. Ultrason. Geol. Proc. Inst. Electron. Eng. 53, 129–133.
Steiger, M., 2005. Crystal growth in porous materials. I: the crystallization pressure of large crystals. J. Cryst. Growth 282, 455–469.
Tamrakar, N.K., Shuichiro, Y., Shrestha, S.D., 2007. Relationships among mechanical, physical and petrographic properties of Siwalik sandstones, Central Nepal Sub-Himalayas. Eng. Geol. 90, 105–123.
UNE-EN 12370, 2002. Natural stone test methods. Determination of resistance to salt crystallization. AENOR, Madrid.
UNE-EN 12371, 2011. Natural stone test methods. Determination of frost resistance. AENOR, Madrid.

UNE-EN 12372, 2007. Natural stone test methods. Determination of flexural strength under concentrated load. AENOR, Madrid.
UNE-EN 13755, 2008. Natural stone test methods. Determination of water absorption at atmospheric pressure. AENOR, Madrid.
UNE-EN 15886, 2011. Conservation of cultural property. Test methods. Colour measurement of surfaces. AENOR, Madrid.
UNE-EN 1925, 2000. Natural stone test methods. Determination of water absorption coefficient by capillarity. AENOR, Madrid.
UNE-EN 1926, 2007. Natural stone test methods. Determination of uniaxial compressive strength. AENOR, Madrid.
UNE-EN 1936, 2007. Natural stone test methods. Determination of real density and apparent density, and of total and open porosity. AENOR, Madrid.
Vereecken, E., Roels, S., 2013. Hygric performance of a massive masonry wall: how do the mortar joints influence the moisture flux? Constr. Build. Mater. 41, 697–707.
Vergès-Belmin, V., 2008. Illustrated Glossary on Stone Deterioration Patterns = Glossaire illustré sur les formes d'altération de la pierre, English-French ed. Monuments & Sites 15. ICOMOS (International Council on Monuments and Sites) and ISCS (International Scientific Committee for Stone), Paris (80 pp.).
Viseras, C., Soria, J.M., Fernández, J., 2004. Cuencas Neógenas Postorogénicas de la Cordillera Bética. In: Vera, J.A. (Ed.), Geología de España. SGE-IGME, Madrid, pp. 576–581.
Whitney, D.L., Evans, B.W., 2010. Abbreviations for names of rock-forming minerals. Am. Mineral. 95, 185–187.
Xiao, Y., Fu, X., Gu, H., Gao, F., Liu, S., 2014. Properties, characterization and decay of sticky rice-lime mortars from the Wugang Ming Dynasty City Wall (China). Mater. Charact. 90, 164–172.
Zorlu, K., Gokceoglu, G., Ocakoglu, F., Nefeslioglu, H.A., Acikalin, S., 2008. Prediction of uniaxial compressive strength of sandstones using petrography-based models. Eng. Geol. 96, 141–158.